Quadrilateral-patterned perforated gas diffusion layers boost the performance of fuel cells

Pengzhu Lin[a,1], Jing Sun[a,1], Changxiang He[a], Maochun Wu[b,*], Tianshou Zhao[a,c,*]

[a] Department of Mechanical and Aerospace Engineering, The Hong Kong University of Science and Technology, Clear Water Bay, Kowloon, Hong Kong SAR, China

[b] Department of Mechanical Engineering, The Hong Kong Polytechnic University, Hung Hom, Kowloon, Hong Kong SAR, China

[c] Department of Mechanical and Energy Engineering, Southern University of Science and Technology, Shenzhen, 518055, China

Abstract

Water flooding remains a critical challenge that hinders the operation of fuel cells at high current and power densities. Here, we develop a novel gas diffusion layer (GDL) featuring quadrilateral-patterned perforations to boost the water drainage capability in proton exchange membrane fuel cells. When the perforations are vertically arranged to flow channels, the fuel cell can achieve a peak power density of 1.43 W cm^{-2} and a current density of as high as 5400 mA cm^{-2}, far outperforming those with commercial GDLs with and without a microporous layer by 28.6% and 58.8%, respectively. Pore-scale simulations reveal the patterned perforations reduce the breakthrough pressure and facilitate water removal, thus improving oxygen diffusion in the perforated GDLs, while cell-scale simulations show that the vertically arranged perforations to flow channels significantly enhance water removal to the adjacent channels due to the improved in-plane permeability, thereby reducing liquid water saturation and boosting cell performance.

* Corresponding authors
E-mail addresses:
maochun.wu@polyu.edu.hk (M.C. Wu), zhaots@sustech.edu.cn (T.S. Zhao).
[1] These authors contributed equally to this work.

TOC graphic:

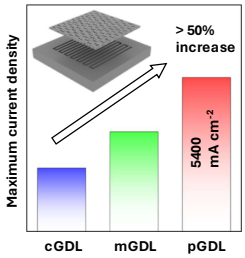
> 50%
increase
Maximum current density
5400
mA cm-2
cGDL
mGDL
pGDL

Fuel cells, particularly proton exchange membrane fuel cells (PEMFCs), have emerged as one of the most promising candidates for next-generation power sources owing to their exceptional energy efficiency, remarkable power density, and zero emission [1–3]. Although commercial applications for transportation and stationary power generation have been demonstrated, wide market penetration of fuel cells is still hindered by cost issues, primarily due to the use of expensive key components such as Pt/C catalyst and proton exchange membranes (PEMs) [4,5]. Increasing operating current and power densities can reduce stack size and thus reduce the capital cost. However, at high current densities, considerable water will be produced by oxygen reduction reaction, which will occupy the pores and block the transport pathways of gas reactants (a phenomenon well known as water flooding), and consequently deteriorate the performance of the PEMFCs dramatically [6–9].

Gas diffusion layers (GDLs) are commonly employed in fuel cells to drain water out from catalyst layers (CLs) and facilitate the uniform feed of gas reactants from the flow channels to the active sites in CLs [6,7]. To facilitate the removal of liquid water, hydrophobic treatment is commonly applied by using hydrophobic agents such as polytetrafluoroethylene (PTFE) and fluorinated ethylene propylene (FEP) [6,10–13]. To tailor the surface wettability, Forner-Cuenca developed a GDL with pattern wettability by radiation-induced grafting of hydrophilic compounds onto the hydrophobic polymer coating, which provided water removal highway in hydrophilic areas [14,15]. Wen et al. developed a Janus GDL which facilitated water removal from the hydrophobic side to the hydrophilic side with low water breakthrough pressure [16]. The transport of liquid water from CLs through GDL to the flow channels is mainly driven by capillary force induced by the stochastic hydrophobic carbon fibers, where a substantial breakthrough pressure is required to expel water. Given that liquid water usually follows the path of least resistance in the porous media, its transport tends to be unpredictable

and undirected within the GDL with complex porous structure. Therefore, GDLs remain susceptible to water flooding during high-current-density operation.

To tackle this challenge, considerable efforts have been devoted to engineering the porous structure of GDLs for enhancing water removal capability over the past several decades [6,7]. One approach involves the implementation of gradient porosity (increasing from microporous layer to flow channel), which has shown great potential in preventing excessive flooding within the GDLs [17]. However, most of the research on GDLs with gradient porosity in fuel cells has been limited to numerical investigations [17–19], with only a few experimental demonstration [20]. This is probably because the manufacture of carbon-based GDLs with gradient porosity is very challenging. Unlike gradient GDLs which are difficult to manufacture, perforation represents a more viable strategy to modify porous structures. Several studies have investigated the effects of GDL perforations on the PEMFC performance and indicated that the massive heat generated during the perforation process can oxidize the nearby region around pores and lead to hydrophilic pores within the PTFE-coated GDLs [21–23]. These hydrophilic pores can create pathways for water removal due to capillary pressure. However, it is found that more liquid water accumulates around the hydrophilic pores, resulting in continuous liquid water coverage near the CLs, thus hindering gas transport and deteriorating cell performance [24]. Therefore, wet-proofing the GDLs after laser-structuring step should be adopted. With the same hydrophobicity, the size and shape of perforations also influence the water removal process. Recently, Csoklich et al. investigated the effects of perforations of GDL by using a series of 16 perforations with different sizes and shapes [11]. The perforation area ratio was found to play a crucial role, as the performance of the fuel cell initially increased and then decreased with an increasing perforation area ratio (volcano-like plots). This behavior can be attributed to the fact that an increase in the perforation area ratio improves water transport and reduces oxygen transport resistance, but it also leads to an increase in high-frequency resistance (HFR)

due to membrane dehydration. Unfortunately, the results were obtained under high flow rates (0.6 L min^{-1} cm^{-2}), which may not be practical for real-world applications. Additionally, the underlying two-phase transport mechanism with perforations remains elusive, hindering the further development of high-performance perforated GDLs for high current and power density fuel cells.

Herein, we propose and demonstrate a perforated GDL (pGDL) to enhance water management in PEMFCs via a facile laser drilling method (Figure 1a). As illustrated in Figure 1b, our proposed pGDL features quadrilateral-patterned perforations that are arranged vertically to the flow channels. This unique design creates highways for liquid water removal and considerably promotes oxygen transport (Figure 1c), thereby significantly enhancing the cell performance. It is experimentally demonstrated that the fuel cell can deliver a peak power density of 1.43 W cm^{-2} and a maximum current density of 5400 mA cm^{-2}, far surpassing the commercial benchmark GDLs which suffer from significant concentration losses.

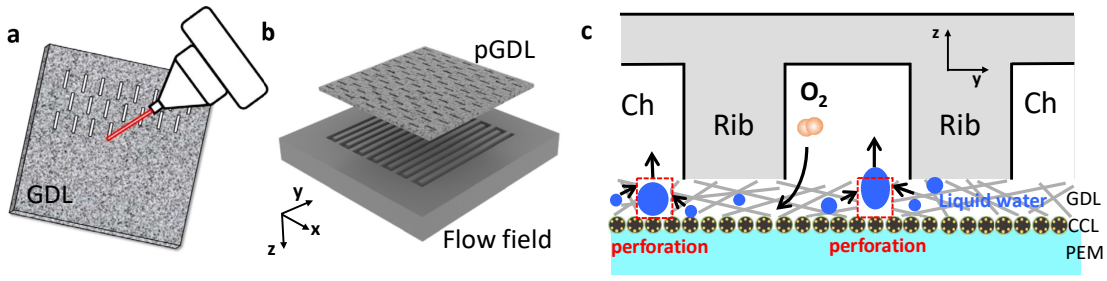

Figure 1. Schematic diagrams of (a) laser drilling for perforation, (b) arrangement of perforated GDL and flow field, and (c) two-phase mass transport in PEMFCs with perforated GDL.

Figure 2a presents a representative image of pGDL featuring quadrilateral-patterned perforations with high-aspect-ratio. This specific pGDL sample is obtained from a 10 cm × 10 cm carbon paper substrate (Figure S1). Utilizing the laser drilling method, we can fabricate 16 individual pGDLs on the carbon paper with controllable patterned perforations, indicating the exceptional scalability of the laser drilling method for perforating GDLs. The porous structures of GDLs were characterized with computed tomography (CT). Volume-rendered tomographic

reconstructions for different GDLs are presented in Figure 2b and c after reconstruction and segmentation of a series of CT images. Commercial GDL (cGDL) mainly consists of carbon fibers that are randomly connected and arranged in a layered structure, forming an interconnected pore network between fibers. In contrast, the pGDL not only exhibits random inter-fiber pores but also incorporates laser perforations in rectangular shapes. Equivalent pore and throat size can provide a quantitative description of the pore network structure in porous media. The equivalent pore and throat size distribution shown in Figure 2d and e reveal that pGDL possesses not only smaller inter-fiber pores, but also larger pores with equivalent diameters exceeding 300 μm created by laser perforation. The distribution of porosity along the in-plane y direction is calculated based on the Porespy code and shown in Figure 2f. The porosity of cGDL is distributed around 0.7 and fluctuates within a range of 0.1, while that of pGDL rapidly increases in the central region, which aligns perfectly with the region of laser perforations.

The morphology of pGDL was also characterized by scanning electron microscopy (SEM) with energy dispersive X-ray spectroscopy (EDS) mapping, as shown in Figure 2g-i. The laser perforations with a high aspect ratio are uniformly distributed across the porous GDL. EDS mapping shows that fluorine and carbon elements are uniformly distributed, indicating the uniform coating of PTFE, which can prevent a decrease in hydrophobicity due to surface oxidation during the laser drilling process. In addition, mercury intrusion porosimetry (MIP) measurements reveal that the primary pores for both cGDL and GDL with microporous layer (mGDL) are in the range of 30-50 μm (Figure 2j). In contrast, in addition to these intrinsic pores of Toray-60 carbon paper, pGDL also exhibits 50-100 μm pores and non-negligible pores above 100 μm that are attributed to the rectangular shape of the laser-perforated pores with a high aspect ratio. It should be noted that the proportion of laser-perforated pores is less than 10%, resulting in a low volume fraction of these larger pores to maintain its mechanical strength

and electrical contact with flow field. Moreover, the cGDL and pGDL exhibit excellent hydrophobic properties (Figure 2k and l) with contact angles of 147.9° and 130.5°, respectively.

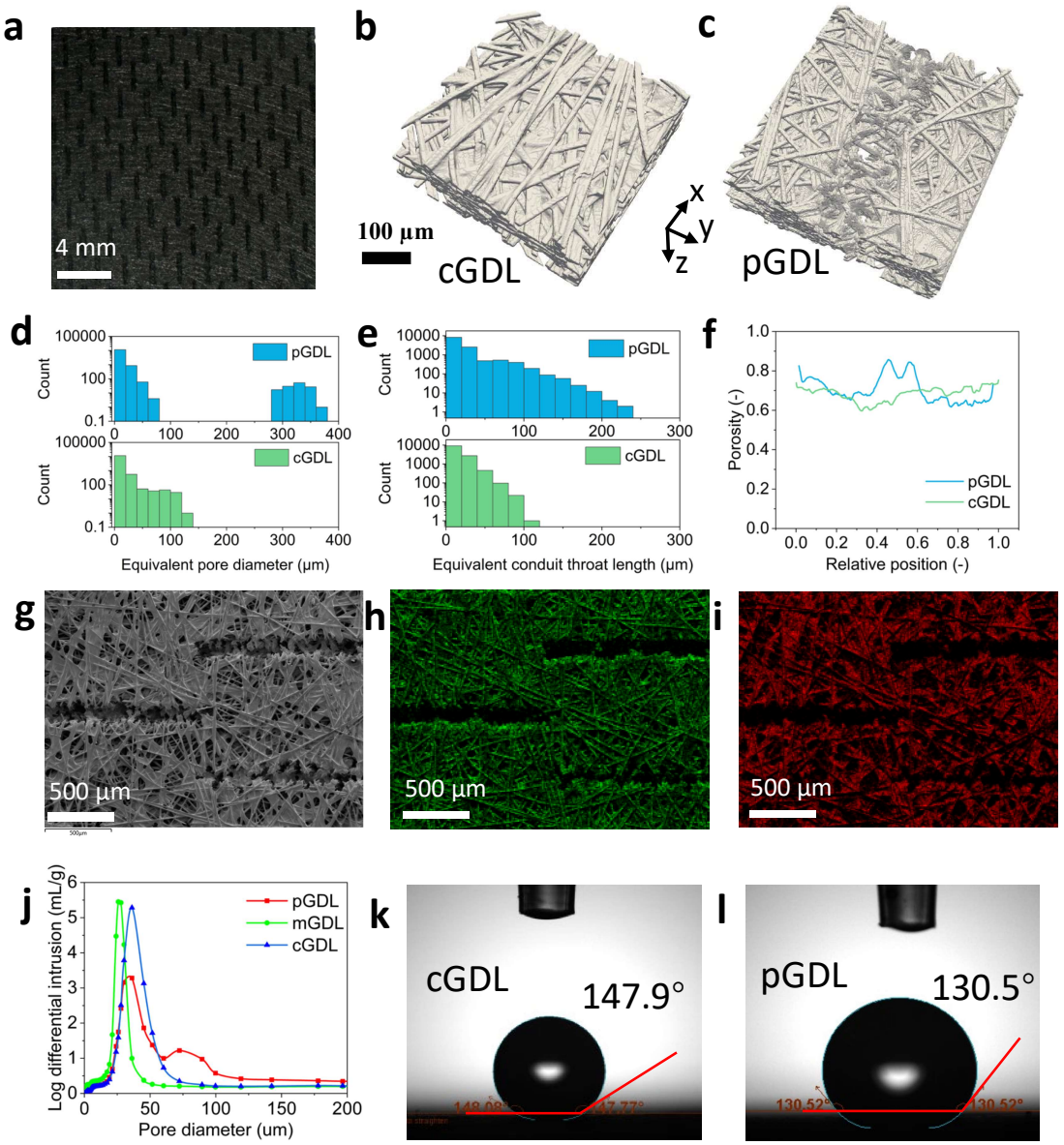

Figure 2. Characterizations of GDL. (a) Digital image of the representative pGDL by laser drilling method. Volume rendering of (b) mGDL and (c) pGDL by computed topography characterization. Statistical analysis of porous structure by (c) equivalent pore diameter, (d) equivalent conduit throat length, and (e) porosity distribution. (g) SEM image, (h-i) EDS mapping of pGDL. The green color denotes the carbon element, while the red color denotes

the fluorine element. (j) Pore size distribution of different GDLs characterized by MIP. Contact angle of water droplet on (k) cGDL and (l) pGDL.

The as-prepared pGDL was then tested in a lab-made PEMFC under 80 °C, 150 kPa, 95% relative humidity and H_2-air condition with a stoichiometric ratio of 3. First, we investigated the effects of three different arrangements (vertical, parallel, and oblique shown in Figure 3a) of the patterned perforations of pGDLs on fuel cell performance. Polarization curves in Figure 3b clearly indicate that the orientation of the patterned perforations has a significant impact on the cell performance, particularly under high current densities. Specifically, the vertical arrangement of pGDL to flow channels exhibits the smallest concentration loss, while it is the highest in parallel configuration (underly mechanisms are further discussed in the full-cell simulation section). Therefore, pGDLs with vertical-to-channels arrangement were adopted for further experimental investigation. As shown in Figure 3c, the PEMFC with pGDL exhibits the best performance under high current density compared to those with mGDL and cGDL. The latter two cells suffer from significant performance loss due to severe concentration overpotentials. Under current density over 3000 mA cm^{-2}, excessive water generation blocks the pathway in GDL and hinders oxygen transport, leading to a substantial voltage drop in PEMFCs with mGDL and cGDL. The HFR-free results of polarization curves in Figure S2 show the same tendency. It is interesting to find that the PEMFC with cGDL exhibits the lowest high-frequency resistance and ohmic losses compared to the other two cells, which is probably attributed to its higher membrane hydration due to poorer water drainage capability. However, as the current density is further increased, water flooding significantly deteriorates its performance due to increased concentration overpotential. Water flooding is alleviated in PEMFC with mGDL because the microporous layer in mGDL can reduce the water breakthrough pressure and facilitate the removal of liquid water within the complex porous medium. Compared with mGDL and cGDL, pGDL leads to the smallest

concentration overpotential as the patterned perforations provide highways for rapid liquid water removal. Remarkably, the PEMFC with pGDL exhibits a peak power density of 1.43 W cm^{-2}, far exceeding those with mGDL and cGDL (1.29 and 1.38 W cm^{-2}). Moreover, the PEMFC with pGDL delivers a maximum current density of as high as 5400 mA cm^{-2}, which is 28.6% and 58.8% higher than those with mGDL and cGDL, respectively. In addition, our pGDLs enable a stable output current at constant voltage discharge, representing a better water management capability (Figure S3). To demonstrate the superiority of our design, we compare the current densities at 0.4 V with other related works under different specific flow rates [11,21,22,25–27]. We adopted two flow rates to operate PEMFCs, namely a relatively low flow rate with a stoichiometric ratio of 3 and a higher constant flow rate of 0.375 NL min^{-1} cm^{-2}. As shown in Figure 3d, PEMFCs developed in this work outperform most reported works even at a relatively low flow rate. The fuel cell with pGDL can achieve even better performance (39.5% increase) at the higher flow rate (0.375 L min^{-1} cm^{-2}), demonstrating the superb liquid water drainage capability of pGDL. Nevertheless, in practical applications, it is common to employ relatively low flow rates (e.g., a stoichiometric ratio of 3) to ensure optimal energy efficiency of the entire fuel cell system, and it is hence adopted in this work.

Figure 3e and f display the electrochemical impedance spectra (EIS) obtained under low current density (LCD) and high current density (HCD). The Nyquist plots in Figure 3e primarily exhibit two arcs, corresponding to the charge transfer and mass transfer resistance, which are related to proton conduction and oxygen transport in fuel cells, respectively. For cGDL and mGDL, increasing the operating current density results in a significant increase in the second arc, representing the increased mass transport resistance. In contrast, the impedance plot of pGDL in red color shown in the inset shows a smaller increase in the second arc after increasing the current, highlighting its superior water drainage capability. To quantitatively analyze the EIS results, the impedance was further fitted by an equivalent circuit as shown in

Figure 3f, which consists of high-frequency resistance (R_{HF}), charge transfer resistance (R_{CT}), mass transfer resistance (R_{MT}) and corresponding capacities. Increasing the operating current density in PEMFCs leads to the generation of more liquid water. On the one hand, the higher water content enhances the hydration and thus the conductivity of the proton exchange membrane, resulting in a lower charge transfer resistance. On the other hand, the increased liquid water content hinders the diffusion of oxygen in the GDL, leading to a significant increase in mass transfer resistance. It can be observed that the mass transfer resistance of pGDL only increases by 6.6 mΩ from LCD to HCD, which is much lower than the corresponding increases of 32.5 and 335.6 mΩ for mGDL and cGDL, respectively. These results confirm the superior water removal capability of pGDL.

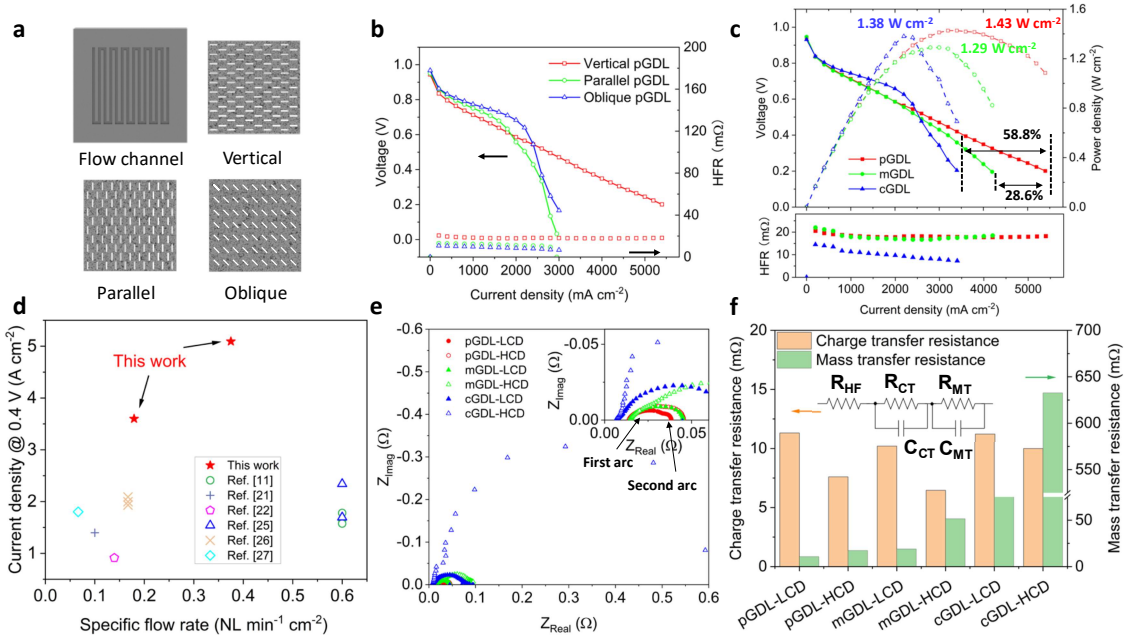

Figure 3. (a) Schematic of serpentine flow channel and different arrangement of pGDL. Polarization curves of PEMFCs (b) with different arrangement and (c) with pGDL and benchmark GDLs. The fuel cells were tested at 80 °C, 150 kPa, 95% relative humidity with a stoichiometric ratio of 3 under H_2-air conditions. (d) Performance comparison of our pGDL to

other reported advanced GDLs. (e) Nyquist plots. (f) Fitting results of PEMFCs with various GDLs under low and high current densities.

To reveal the underlying mechanisms that lead to boosted liquid water removal in pGDLs, pore-scale time-dependent two-phase invasion percolation (IP) and diffusion simulations were performed. The computational domains were derived from computed topography results with segment and smooth treatment, as depicted in Figure S4. Figure 4a and d present the liquid water saturation in cGDL and pGDL, respectively. In the simulation, liquid water seeks breakthrough points (BP) along paths of least resistance, resulting in the occupation of a significant portion of the internal regions in GDLs and forming liquid water pathway. As shown in Figure 4a, the breakthrough occurs on the right side for cGDL. In contrast, liquid water easily flows along perforated paths, leading to efficient drainage, and thus noticeable reduction of liquid water occupation in most areas (Figure 4d). The pressure distributions shown in Figure 4b and e reveal that the pressure within pGDL is significantly lower than that within cGDL, indicating the easier removal of liquid water. Specifically, the breakthrough pressure in pGDL is significantly reduced by 93.5% (Figure 4g). Figure 4c and f depict the velocity distribution and streamlines in GDLs. It can be seen that most of the inlet flow follows the pathway with low pressure and passes through breakthrough points. Additionally, the velocity within the major pathway of the pGDL exhibits a more uniform distribution compared to cGDL. We also simulated oxygen diffusion within liquid-water saturated GDLs. The smaller average liquid saturation shows that there is less liquid water accumulated in pGDL (Figure 4h). In the meantime, as shown in Figure 4i, the average oxygen concentration within the whole region increases over time and eventually reaches a steady state. Interestingly, the average oxygen concentration in pGDL is slightly smaller in the initial stage (< 100 μs), primarily due to the smaller unsaturated oxygen inlet area at the top boundary compared to cGDL. However, it subsequently exhibits a faster growth rate than cGDL and ultimately achieves a higher

average oxygen concentration, which is more favorable for enhancing the performance of fuel cells.

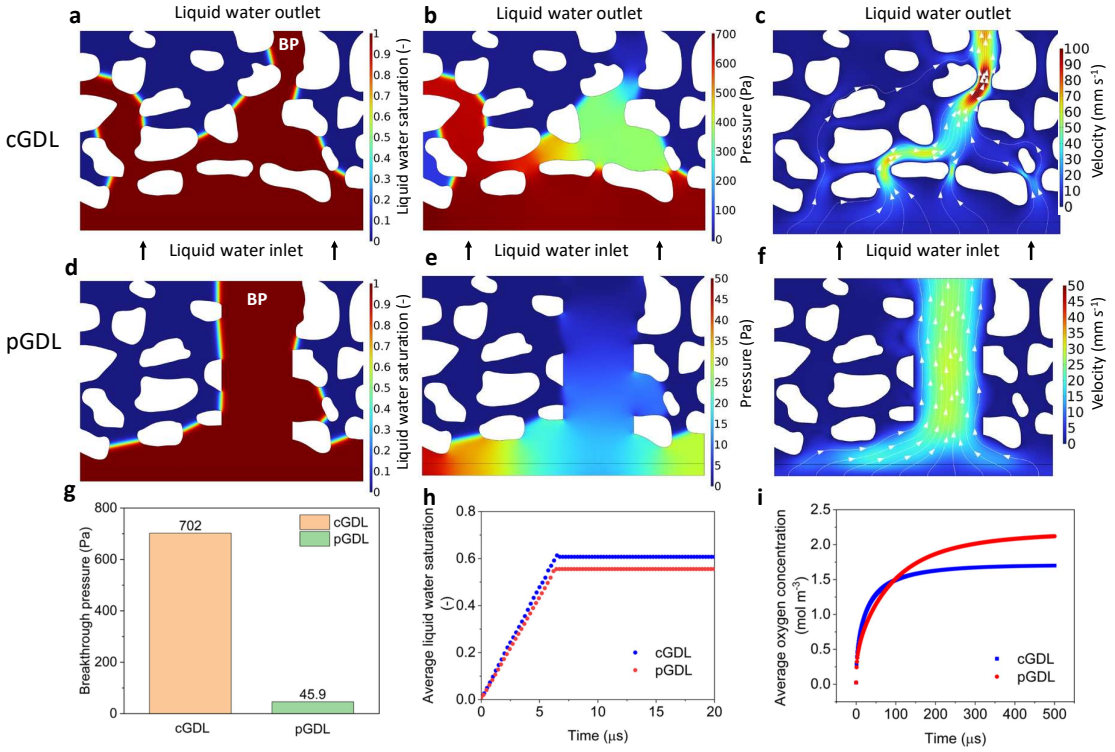

Figure 4. Pore-scale invasion percolation and diffusion simulations. Distribution of (a) liquid water saturation, (b) pressure, and (c) velocity within cGDL. Distribution of (d) liquid water saturation, (e) pressure, (f) velocity within cGDL. Comparison of (g) breakthrough pressure, (h) average liquid saturation, and (i) average oxygen concentration in different GDLs.

To gain a deeper fundamental understanding of the two-phase transport phenomena in GDLs, a three-dimensional two-phase fuel cell model was built by incorporating the pore-scale model. Figure 5a shows the computational domains of three-dimensional fuel cell model with a typical serpentine flow field. The anisotropic permeabilities of both the pGDL and the cGDL were calculated through pore-scale simulations. Figure S5 shows the reconstructed structure of pGDL and cGDL. Anisotropic permeability results are listed in Table S1. Figure 5b shows the quadrilateral-patterned perforations, which are arranged vertically to channels, can significantly improve the x-direction permeability. The calculated permeability values were

subsequently incorporated into the fuel cell model to assess the impact of the GDLs on the transport of liquid water within the fuel cell system. Figure 5c-e show the distribution of liquid water saturation on the interface between GDLs and channels/ribs. For cGDL, liquid water mainly accumulates under the ribs, which is consistent with in-situ observation of liquid water distribution reported in previous works [28]. This phenomenon occurs due to the significant difference in the travel distance for liquid water to reach the channel outlet. Liquid water under the rib needs to go through long distances (several millimeters in x direction) to reach channel while liquid water under the rib only needs to go through several micrometers in z direction. Therefore, perforation areas provided by pGDLs can enhance water transport in x direction by placing the high-aspect-ratio perforation vertical to channels. Accordingly, the use of vertical pGDL results in a significant reduction in liquid water saturation (Figure 5d) due to the improved permeability in the x-direction. The enhanced permeability in the x-direction facilitates the transport of liquid water towards nearby flow channels, thus enabling effective water drainage. To compare the influence of pGDL arrangement on liquid water distribution, Figure 5e displays the distribution of liquid water when pGDL is arranged in a parallel direction. It can be observed that the parallel arrangement leads to enhanced permeability in the y-direction improves drainage in that direction. Consequently, the accumulation of liquid water in the lower-left and upper-left corners is notably reduced. However, there is still remarkable liquid water accumulation in the under-rib regions between the channels. Overall, the improvement in drainage performance with parallel pGDL arrangement is not significant, which is consistent with the large concentration loss in the cell performance (Figure 3b). Figure 5f displays the average liquid water saturation of GDLs under different operating voltages. When the voltage drops below 0.7 V, the average liquid water saturation increases significantly with voltage owing to the substantial generation of water in the cathode CL. However, since

pGDL can remove liquid water more effectively, the average liquid water saturation is much lower compared to that of cGDL (reduced by 20.5% at a cell voltage of 0.2 V).

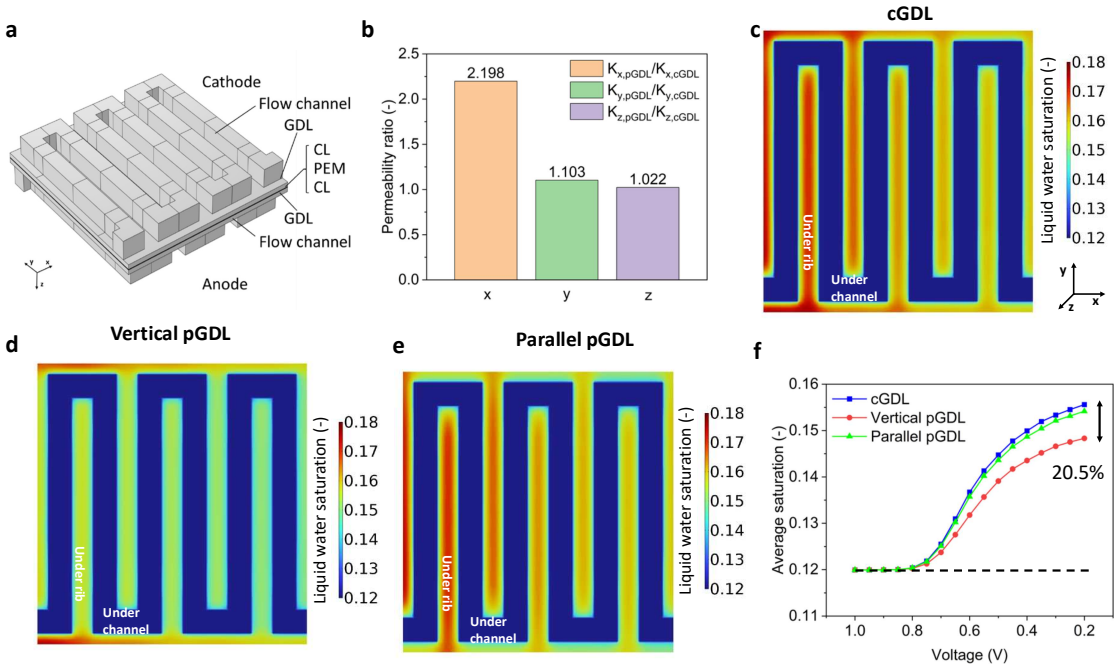

Figure 5. Full cell modeling of PEMFCs. (a) Computational domains for three-dimensional fuel cell modeling. (b) Permeability results of pore-scale simulation of GDLs. Liquid water saturation distribution of (c) cGDL, (d) vertical pGDL, and (e) parallel pGDL. (f) Average liquid water saturation under different voltages.

In summary, a laser-perforated GDL featuring quadrilateral pattern was successfully developed for improving water management in PEMFCs. It is demonstrated that when the patterned high-aspect-ratio perforations are arranged vertically to flow channels, the PEMFC can achieve a peak power density of 1.43 W cm^{-2} and a maximum current density of 5400 mA cm^{-2} under H_2-air condition, far exceeding those with commercial benchmark GDLs due to smaller concentration overpotentials. It is revealed, by pore-scale simulations, that perforations effectively reduce the breakthrough pressure and serve as highways for water removal, which diminishes the overall liquid water saturation and improves oxygen diffusion in pGDL. The three-dimensional two-phase full cell simulations further reveal that the patterned perforations

vertical to flow channels can enhance water transport to nearby channels due to the increased in-plane permeability, resulting in rapid water drainage and thus boosting the cell performance.

Supporting Information:

Experimental details, including material and sample preparation, fuel cell testing, material characterizations, HFR-free results, water management capability results, numerical simulation details, including pore-scale modeling of two-phase transport, pore-scale modeling of anisotropy transport property, and three-dimensional fuel cell modeling.

Acknowledgment

This work described in this paper was supported by grants from the Research Grants Council of the Hong Kong Special Administrative Region, China (Project No. C6011-20G and No. 16205822).

References

(1) Jiao, K.; Xuan, J.; Du, Q.; Bao, Z.; Xie, B.; Wang, B.; Zhao, Y.; Fan, L.; Wang, H.; Hou, Z.; Huo, S.; Brandon, N. P.; Yin, Y.; Guiver, M. D. Designing the next Generation of Proton-Exchange Membrane Fuel Cells. *Nature* **2021**, *595* (7867), 361–369.

(2) Kodama, K.; Nagai, T.; Kuwaki, A.; Jinnouchi, R.; Morimoto, Y. Challenges in Applying Highly Active Pt-Based Nanostructured Catalysts for Oxygen Reduction Reactions to Fuel Cell Vehicles. *Nat. Nanotechnol.* **2021**, *16* (2), 140–147.

(3) Cullen, D. A.; Neyerlin, K. C.; Ahluwalia, R. K.; Mukundan, R.; More, K. L.; Borup, R. L.; Weber, A. Z.; Myers, D. J.; Kusoglu, A. New Roads and Challenges for Fuel Cells in Heavy-Duty Transportation. *Nat. Energy* **2021**, *6* (5), 462–474.

(4) Thompson, S. T.; Papageorgopoulos, D. Platinum Group Metal-Free Catalysts Boost Cost Competitiveness of Fuel Cell Vehicles. *Nat. Catal.* **2019**, *2* (7), 558–561.

(5) Debe, M. K. Electrocatalyst Approaches and Challenges for Automotive Fuel Cells. *Nature* **2012**, *486* (7401), 43–51. https://doi.org/10.1038/nature11115.

(6) Ozden, A.; Shahgaldi, S.; Li, X.; Hamdullahpur, F. A Review of Gas Diffusion Layers for Proton Exchange Membrane Fuel Cells—With a Focus on Characteristics, Characterization Techniques, Materials and Designs. *Prog. Energy Combust. Sci.* **2019**, *74*, 50–102.

(7) Omrani, R.; Shabani, B. Gas Diffusion Layer Modifications and Treatments for Improving the Performance of Proton Exchange Membrane Fuel Cells and Electrolysers: A Review. *Int. J. Hydrog. Energy* **2017**, *42* (47), 28515–28536.

(8) Zhang, G.; Jiao, K. Multi-Phase Models for Water and Thermal Management of Proton Exchange Membrane Fuel Cell: A Review. *J. Power Sources* **2018**, *391*, 120–133.
(9) Chen, Q.; Niu, Z.; Li, H.; Jiao, K.; Wang, Y. Recent Progress of Gas Diffusion Layer in Proton Exchange Membrane Fuel Cell: Two-Phase Flow and Material Properties. *Int. J. Hydrog. Energy* **2021**, *46* (12), 8640–8671.
(10) Sarker, M.; Rahman, M. A.; Mojica, F.; Mehrazi, S.; Kort-Kamp, W. J. M.; Chuang, P.-Y. A. Experimental and Computational Study of the Microporous Layer and Hydrophobic Treatment in the Gas Diffusion Layer of a Proton Exchange Membrane Fuel Cell. *J. Power Sources* **2021**, *509*, 230350.
(11) Csoklich, C.; Schmidt, T. J.; Büchi, F. N. High Performance Gas Diffusion Layers with Added Deterministic Structures. *Energy Environ. Sci.* **2022**, *15* (3), 1293–1306.
(12) Niu, Z.; Bao, Z.; Wu, J.; Wang, Y.; Jiao, K. Two-Phase Flow in the Mixed-Wettability Gas Diffusion Layer of Proton Exchange Membrane Fuel Cells. *Appl. Energy* **2018**, *232*, 443–450.
(13) Lin, G.; Nguyen, T. V. Effect of Thickness and Hydrophobic Polymer Content of the Gas Diffusion Layer on Electrode Flooding Level in a PEMFC. *J. Electrochem. Soc.* **2005**, *152* (10), A1942.
(14) Forner-Cuenca, A.; Biesdorf, J.; Lamibrac, A.; Manzi-Orezzoli, V.; Büchi, F. N.; Gubler, L.; Schmidt, T. J.; Boillat, P. Advanced Water Management in PEFCs: Diffusion Layers with Patterned Wettability II. Measurement of Capillary Pressure Characteristic with Neutron and Synchrotron Imaging. *J. Electrochem. Soc.* **2016**, *163* (9), F1038.
(15) Forner-Cuenca, A.; Biesdorf, J.; Gubler, L.; Kristiansen, P. M.; Schmidt, T. J.; Boillat, P. Engineered Water Highways in Fuel Cells: Radiation Grafting of Gas Diffusion Layers. *Adv. Mater.* **2015**, *27* (41), 6317–6322.
(16) Wen, Q.; Pan, S.; Li, Y.; Bai, C.; Shen, M.; Jin, H.; Ning, F.; Fu, X.; Zhou, X. Janus Gas Diffusion Layer for Enhanced Water Management in Proton Exchange Membrane Fuel Cells (PEMFCs). *ACS Energy Lett.* **2022**, *7* (11), 3900–3909.
(17) Kong, I. M.; Jung, A.; Kim, Y. S.; Kim, M. S. Numerical Investigation on Double Gas Diffusion Backing Layer Functionalized on Water Removal in a Proton Exchange Membrane Fuel Cell. *Energy* **2017**, *120*, 478–487.
(18) Huang, Y.-X.; Cheng, C.-H.; Wang, X.-D.; Jang, J.-Y. Effects of Porosity Gradient in Gas Diffusion Layers on Performance of Proton Exchange Membrane Fuel Cells. *Energy* **2010**, *35* (12), 4786–4794.
(19) Wang, Y.; Wang, X.; Qin, Y.; Zhang, L.; Wang, Y. Three-Dimensional Numerical Study of a Cathode Gas Diffusion Layer with a through/in Plane Synergetic Gradient Porosity Distribution for PEM Fuel Cells. *Int. J. Heat Mass Transf.* **2022**, *188*, 122661.
(20) Zhang, Y.; Verma, A.; Pitchumani, R. Optimum Design of Polymer Electrolyte Membrane Fuel Cell with Graded Porosity Gas Diffusion Layer. *Int. J. Hydrog. Energy* **2016**, *41* (20), 8412–8426.
(21) Gerteisen, D.; Heilmann, T.; Ziegler, C. Enhancing Liquid Water Transport by Laser Perforation of a GDL in a PEM Fuel Cell. *J. Power Sources* **2008**, *177* (2), 348–354.
(22) Gerteisen, D.; Sadeler, C. Stability and Performance Improvement of a Polymer Electrolyte Membrane Fuel Cell Stack by Laser Perforation of Gas Diffusion Layers. *J. Power Sources* **2010**, *195* (16), 5252–5257.
(23) Lee, F. C.; Ismail, M. S.; Ingham, D. B.; Hughes, K. J.; Ma, L.; Lyth, S. M.; Pourkashanian, M. Alternative Architectures and Materials for PEMFC Gas Diffusion Layers: A Review and Outlook. *Renew. Sustain. Energy Rev.* **2022**, *166*, 112640.
(24) Markötter, H.; Alink, R.; Haußmann, J.; Dittmann, K.; Arlt, T.; Wieder, F.; Tötzke, C.; Klages, M.; Reiter, C.; Riesemeier, H.; Scholta, J.; Gerteisen, D.; Banhart, J.; Manke, I.

Visualization of the Water Distribution in Perforated Gas Diffusion Layers by Means of Synchrotron X-Ray Radiography. *Int. J. Hydrog. Energy* **2012**, *37* (9), 7757–7761.

(25) Csoklich, C.; Xu, H.; Marone, F.; Schmidt, T. J.; Büchi, F. N. Laser Structured Gas Diffusion Layers for Improved Water Transport and Fuel Cell Performance. *ACS Appl. Energy Mater.* **2021**, *4* (11), 12808–12818.

(26) Wang, X.; Chen, S.; Fan, Z.; Li, W.; Wang, S.; Li, X.; Zhao, Y.; Zhu, T.; Xie, X. Laser-Perforated Gas Diffusion Layer for Promoting Liquid Water Transport in a Proton Exchange Membrane Fuel Cell. *Int. J. Hydrog. Energy* **2017**, *42* (50), 29995–30003.

(27) Manahan, M. P.; Hatzell, M. C.; Kumbur, E. C.; Mench, M. M. Laser Perforated Fuel Cell Diffusion Media. Part I: Related Changes in Performance and Water Content. *J. Power Sources* **2011**, *196* (13), 5573–5582.

(28) Yoshimune, W.; Higuchi, Y.; Kato, A.; Hibi, S.; Yamaguchi, S.; Matsumoto, Y.; Hayashida, H.; Nozaki, H.; Shinohara, T.; Kato, S. 3D Water Management in Polymer Electrolyte Fuel Cells toward Fuel Cell Electric Vehicles. *ACS Energy Lett.* **2023**, *8* (8), 3485–3487.